American Scientific Research Journal for Engineering, Technology, and Sciences (ASRJETS)
ISSN (Print) 2313-4410, ISSN (Online) 2313-4402

http://asrjetsjournal.org/

Definition of a Prototype of High Temperature Synchronous Reluctance Motor

Hamed Elmadah[a]*, Daniel Roger[b], Noureddine Takorabet[c]

[a,c]*Université de Lorraine, Groupe de Recherche en Electrotechnique et Electronique de Nancy (GREEN), 2, avenue de la forêt de Haye 54518 Vandoeuvre lès Nancy, France*
[b]*Université d'Artois, Laboratoire Systèmes Electrotechniques et Environnement, Technoparc Futura, 62400 Béthune, France*
[a]*Email: hamed.elmadah@univ-lorraine.fr*
[b]*Email: daniel.roger@univ-artois.fr*
[c]*Email: noureddine.takorabet@univ-lorraine.fr*

Abstract

This paper discusses the definition of a synchronous reluctance motor with special windings able to work in very hot environments where the ambient temperature rises over 300°C. This motor is designed with inorganic insulated coils able to operate at internal temperatures up to 500°C. With such coils and synchronous reluctance structure, the maximum ambient temperature of using this motor is much over the capabilities of the best magnets. However, this structure has drawback at classical temperatures which it is important to transpose to the extreme temperatures. The paper is dedicated to the construction of a functional prototype which allows the experiments at very high ambient temperatures.

Keywords: High temperature motor; synchronous reluctance motor; non-organic windings; concentrated winding motor.

1. Introduction

The development of the more electric aircraft is now engaged and it accelerates [1-4]. The powers of the electrical networks are becoming larger, many functions now provided by air and hydraulic circuits will be provided by electric actuators, which have better energy efficiency and lower maintenance costs.

---

* Corresponding author.

The more electric aircrafts need powerful actuators and generators placed closer to the main propulsion turbines. Therefore, the development of electric motors able to work in a very hot environment is an important step toward the development of the more electric aircraft. A first prototype of inorganic insulation coils able to work at 500°C has been developed. These coils were mounted on a prototype of permanent magnet motor, which solves the problems of high temperature (HT°) insulation [5]. However, with the best magnets available on the market, it is difficult to work over an ambient temperature of around 250°C considering the losses in the magnets. The main goal is to overcome this lock by defining a motor without magnets. This motor has some disadvantages; it must be magnetized by its stator which involves larger magnetomotive forces (mmf). The objective is to build a prototype able to test the temperature limits of this structure when it is equipped with inorganic coils able to go up to 500°C.

2. Structure of synchronous reluctance motor

2.1. High temperature coils constraints

To build high temperature motor, the use of distributed windings is discarded because of the too complex form imposed on the coils [6]. In fact, the high temperature non-organic coils are coated with cement which able to protect the conductors and contribute to the insulation of the electrical circuit at high temperatures. Therefore, the non-organic coils are rigid and no flexible. Under these conditions, only salient stator equipped with prefabricated coils, may be considered. Figure 1 gives an example of high temperature coil structure mounted on a stator tooth. Thereby, the choice of simple salient synchronous reluctance motor is not possible. Therefore, we propose to study the feasibility of doubly salient synchronous reluctance motor [7]. The HT° wires of the coils are insulated by a very thin ceramic layer. The breakdown voltage of the inter-turns insulation is much lower than the classical organic technology used at lower temperatures. Therefore, the turns must be arranged in order to obtain an optimal distribution of the electrical stresses between the turns. Figure 1 provides an example where the three layers are connected in parallel.

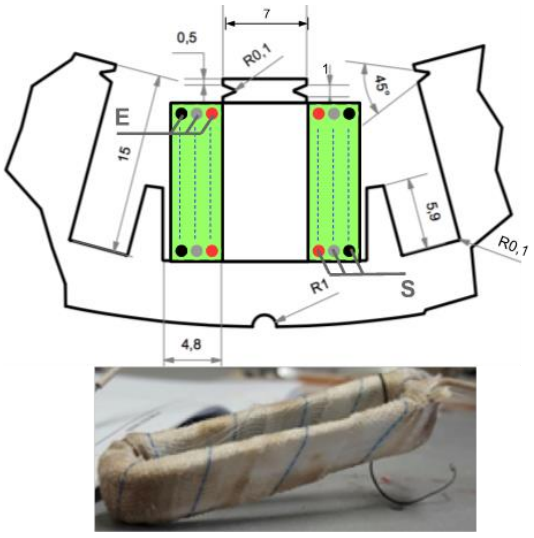

Figure 1: Diagram of the non-organic coil mounted on stator.

The torque ripple is an important parameter to consider; especially since the non-organic insulation of HT° wires are brittle. The important vibrations can damage the coils. It is important to choose a structure that limits the torque ripples without increasing the complexity of the prototype.

2.2. Available topologies for a HT° synchronous reluctance motor

For practical reasons related to the availability of the iron-cobalt stator magnetic circuit designed to operate at HT°, the geometry of the stator is fixed and the number of stator teeth is set to 24. Three possibilities are offered to build the rotor of doubly salient synchronous reluctance motor: 24 coils -16 poles, 24 coils-20 poles or 24 coils-28 poles [8-10]. Figures 2, 3 and 4 show the three topologies and the coils connections of one phase.

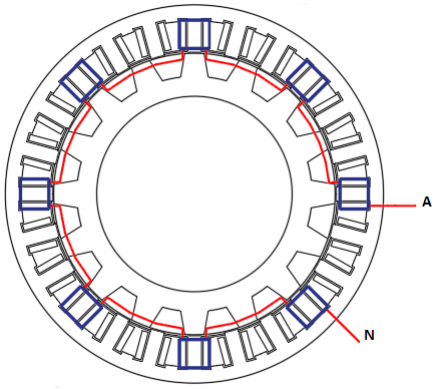

Figure 2: 24 coils 16 poles motor and the coils connections of one phase.

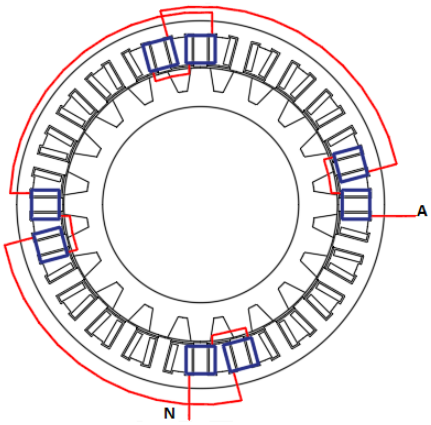

Figure 3: 24 coils 20 poles motor and the coils connections of one phase.

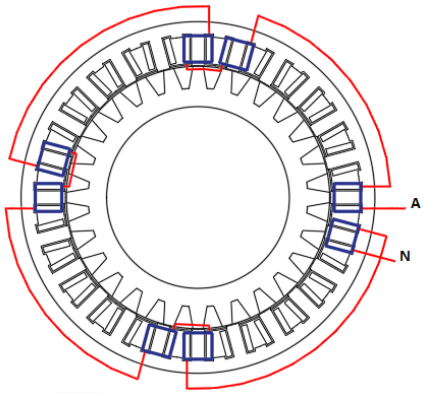

Figure 4: 24 coils 28 poles motor and the coils connections of one phase.

2D simulations by finite elements (FE) are made for the three topologies, with the same geometrical input:

- Outer stator diameter: 160 *mm*;
- Active axial length: 50*mm*;
- Inner stator diameter: 122 *mm*;
- Air gap: 0.7 *mm*;

A specific FE model is developed to model the synchronous reluctance motor by a special approach based on the spectral analysis of inductances. Some precautions have been taken. The mesh around the air gap must be smaller than the other adjacent regions. Figure 5 shows the mesh of the stator teeth, coils and rotor poles.

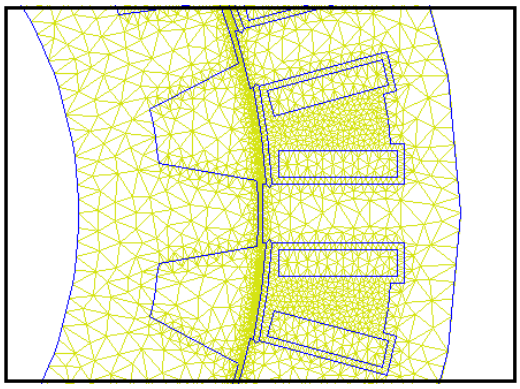

Figure 5: Mesh of the air gap and adjacent regions.

First of all, we adopt the hypothesis of unsaturated materials, which allows establishing an external model using the spectral decomposition of the motor parameters. We calculate the phase fluxes and then we build the inductance matrix [L (θ)] depending on the position of the rotor [11].

$$[L] = \begin{bmatrix} L_{a0} & M_{ab0} & M_{ac0} \\ M_{ab0} & L_{b0} & M_{bc0} \\ M_{ac0} & M_{bc0} & L_{c0} \end{bmatrix} + \sum_n \begin{bmatrix} L_n\cos(2n\theta) & M_n\cos(2n\left(\theta+\frac{2\pi}{3}\right)) & M_n\cos(2n\left(\theta-\frac{2\pi}{3}\right)) \\ M_n\cos(2n\left(\theta+\frac{2\pi}{3}\right)) & L_n\cos(2n\left(\theta-\frac{2\pi}{3}\right)) & M_n\cos(2n\theta) \\ M_n\cos(2n\left(\theta-\frac{2\pi}{3}\right)) & M_n\cos(2n\theta) & L_n\cos(2n\left(\theta+\frac{2\pi}{3}\right)) \end{bmatrix} \quad (1)$$

A single phase is supplied with a constant current, the relationship between the fluxes and the current are determined then the inductances (self and mutual) are calculated by (2).

$$L_A = \left.\frac{\Phi_A}{I_A}\right|_{i_{b,c=0}}$$

$$M_{ab} = \left.\frac{\Phi_B}{I_A}\right|_{i_{b,c=0}} \quad (2)$$

$$M_{ac} = \left.\frac{\Phi_C}{I_A}\right|_{i_{b,c=0}}$$

The inductances are calculated for different values of the rotor position. Figures 6, 7 and 8 show the self-inductance for one phase as the corresponding spectral analysis for the three topologies. The expression of the electromagnetic torque is obtained by derivation of coenergy [12]; it is given by the form:

$$\Gamma = \frac{1}{2}[I]^t \frac{\partial[L]}{\partial\theta}[I] = \Gamma_{ave} + \sum_n \Gamma_{ond}\ \cos(2n\theta + \varphi_n) \quad (3)$$

The approach adopted consists in finding the topology of motor where second term of the inductance matrix is limited to the first harmonic (n=1). In fact, this term is the most important because higher rank harmonics create lower torque ripples.

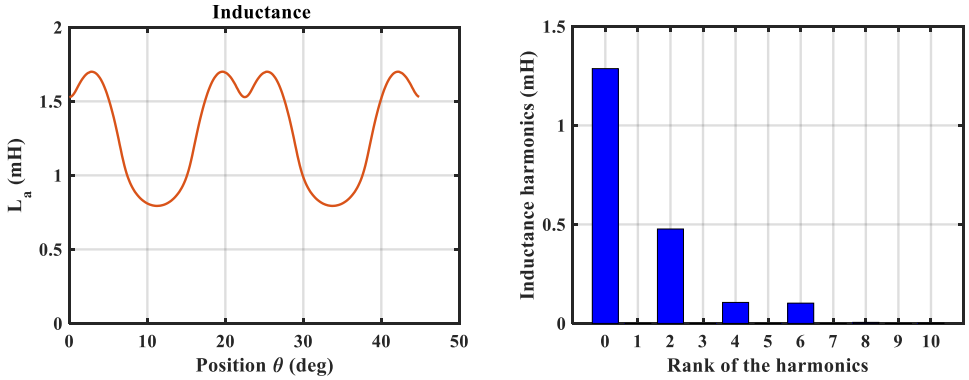

Figure 6: Inductance of a phase and the corresponding Fourier analysis for 24 coils 16 poles motor.

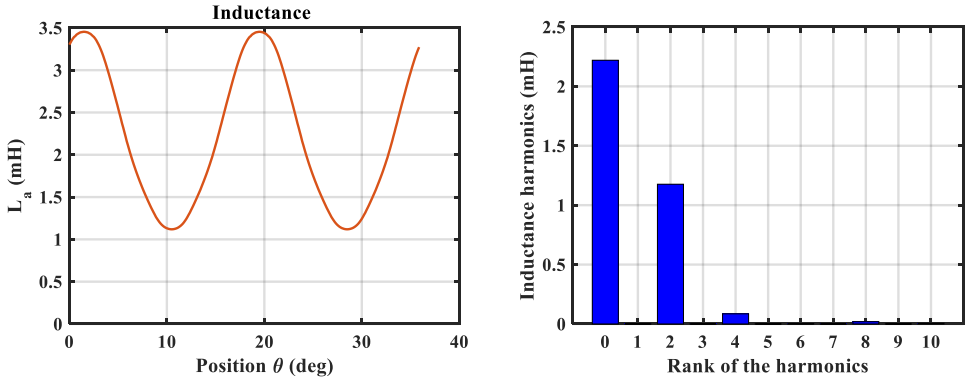

Figure 7: Inductance of a phase and the corresponding Fourier analysis for 24 coils 20 poles motor.

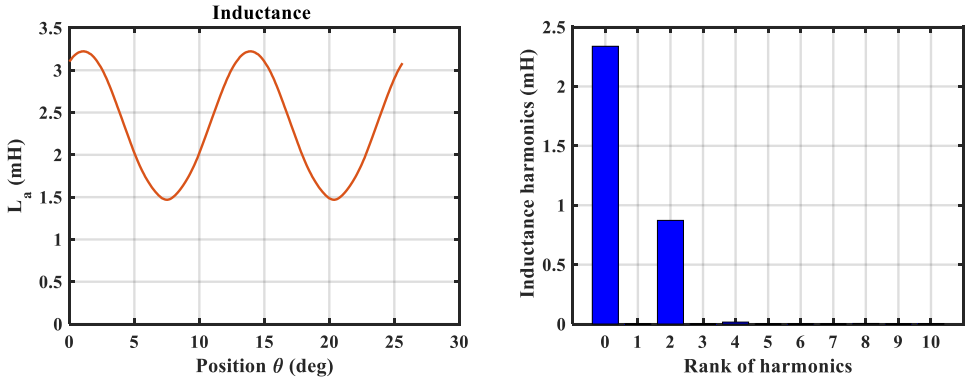

Figure 8: Inductance of a phase and the corresponding Fourier analysis for 24 coils 28 poles motor.

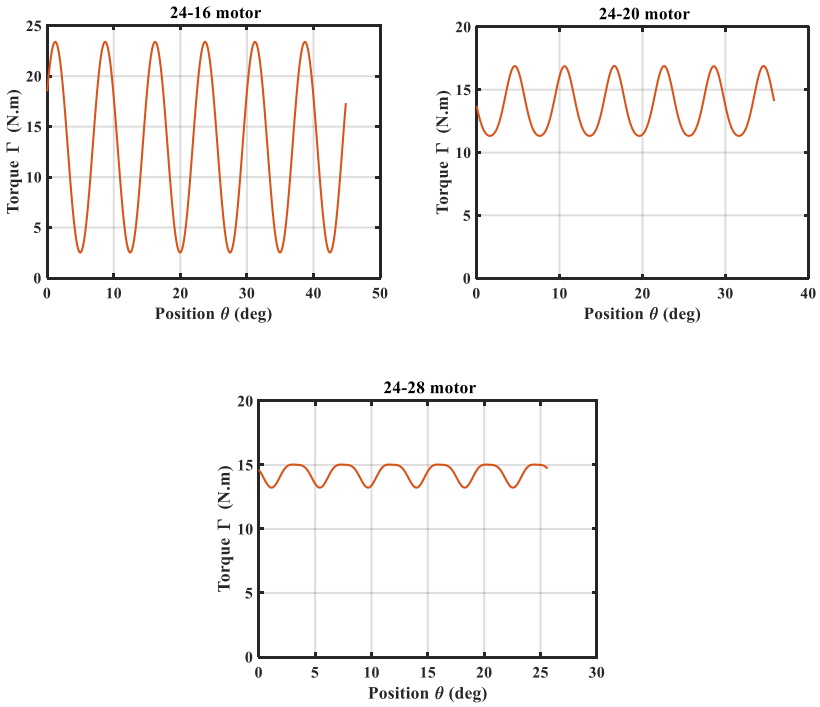

Figure 9: Electromagnetic torque ripples for the three topologies.

Figure 9 shows the calculated torque for the three topologies. The configuration 24 coils -16 poles has a high torque ripple rate, so it is dismissed. The simulations show that the lowest torque ripples are obtained with the configuration 24 coils -28 poles. However, this configuration requires a higher electric frequency at imposed speed because this motor has 14 pairs of poles. Eddy currents (Foucault currents) losses in iron will be higher. Thus, the choice of 24-20 configuration is an acceptable compromise also which has torque ripple lower than 24-16 configuration.

2.3. Geometric optimization

After choosing the topology 24-20, the shape of the rotor teeth must be chosen. An optimization approach is adopted by considering three parameters: the angular opening of rotor teeth, the inclination sides of the teeth and air gap extra thickness. A parametric study made it possible to obtain elements that limit torque harmonics and Figure 10 shows the three optimization parameters.

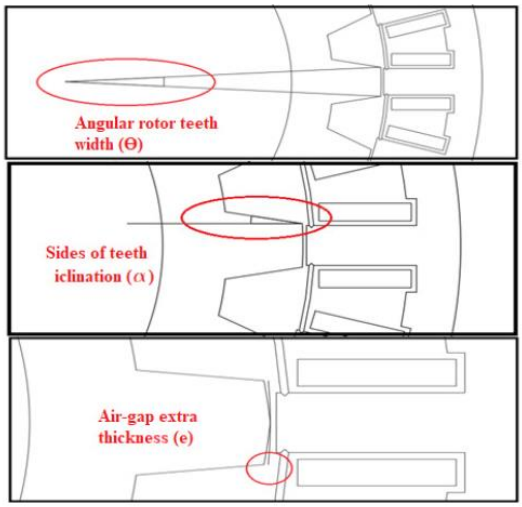

Figure 10: Rotor shape optimization parameters

Figures 11, 12 and 13 show the influence of the three parameters on the harmonics and the torque ripple.

This parametric study allows to identify the influence of these parameters on the torque ripples and to choose a suitable set of parameters. Optimization results are $\theta = 8.1°$, $\alpha = 10°$ and $e = 0.05mm$. A specific design to satisfy the specification which has been implemented. The constraints of high temperature lead to significant manufacturing difficulties. Organic insulation layers between magnetic sheets are forbidden; the sheets must be maintained mechanically. One solution is considered; it's to build a massive rotor with techniques that could reduce eddy current losses in the rotor. Figure 14 shows the geometry of the massive rotor obtained. Longitudinal streaks have been added in the poles to limit eddy currents due to rotating fields created by the mmf harmonics.

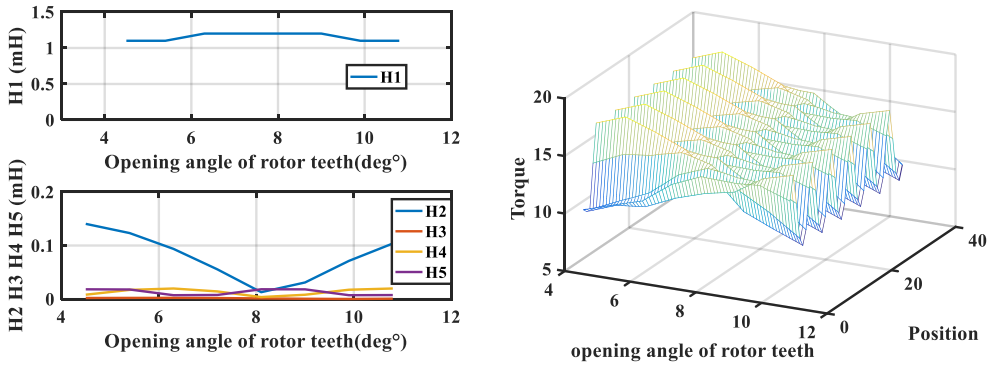

Figure 11: Influence of the angular rotor teeth width on the harmonics and the torque ripple.

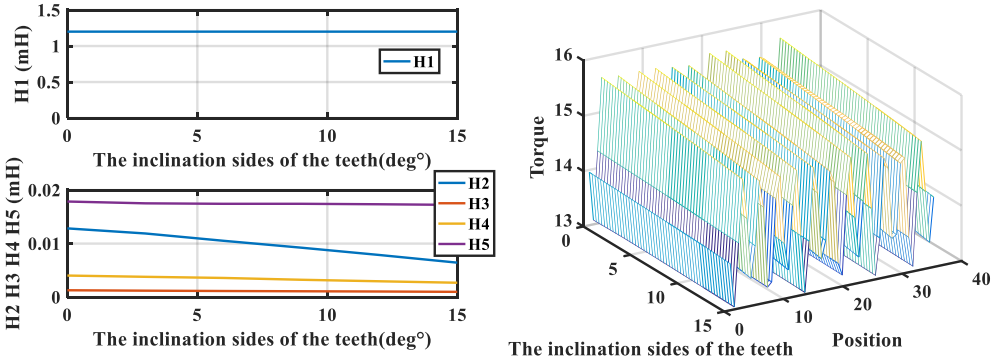

Figure 12: Influence of the inclination sides of the rotor teeth on the harmonics and the torque ripple.

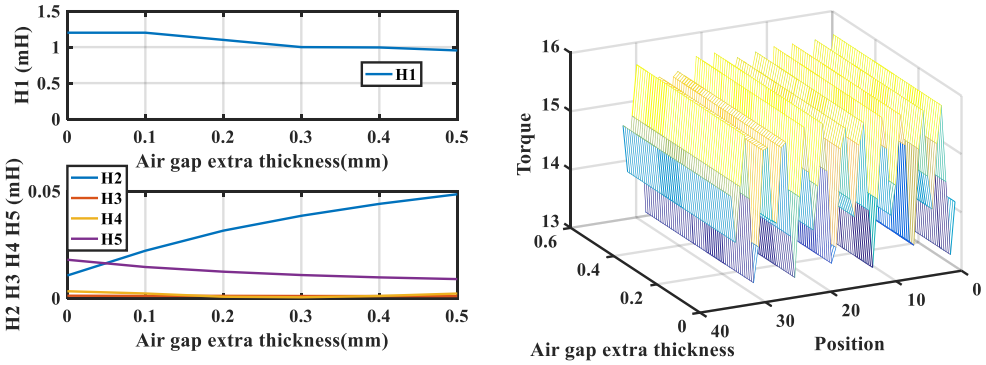

Figure 13: Influence of the Air gap extra thickness on the harmonics and the torque ripple.

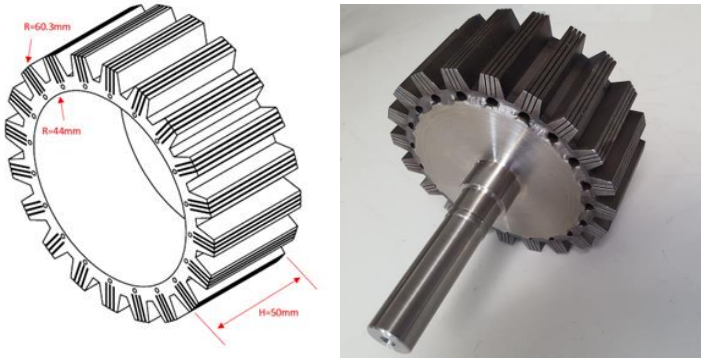

Figure 14: Shape retained for the massive rotor.

The massive rotor has the advantage of being very strong and relatively easy to build with today's machine tools. However, it has a serious defect related to Joules losses due to the currents induced by the harmonic fields due to armature reaction. The backward rotating fields in the opposite direction generate high frequency eddy-currents. The laminated version of the same rotor is shown in Figure 15. Silicon steel sheets insulated by natural oxidation are protected by stainless steel flanges to avoid mechanical problems.

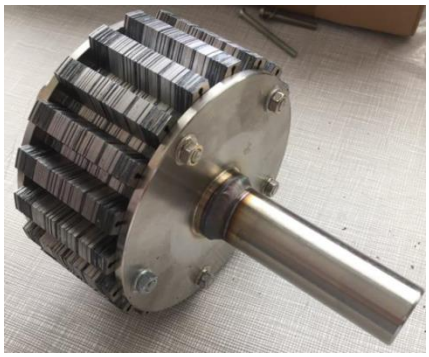

Figure 15: Laminated version.

3. Stator coil design

The coils connections of one phase for 24 coils 20 poles motor are defined in Figure 3. To locate the positions of the magneto-motive force (mmf) created by the currents in the phases, it is necessary to identify all the coils angular positions with respect to a single reference axis taken arbitrarily between the coil 24 and the coil 1 as shown in Figure 16. This reference axis will also be used for the control to position the poles of the (mmf) rotating relative to the poles of the rotor.

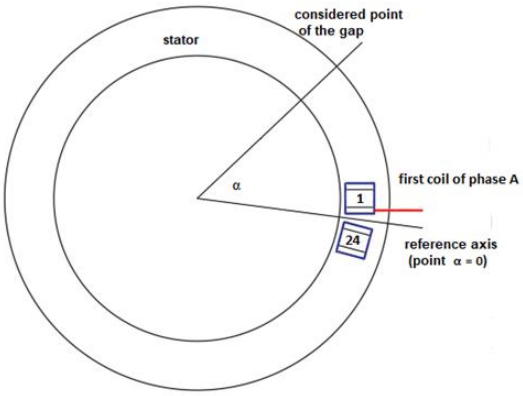

Figure 16: Locating the air gap points with respect to the reference axis.

The instantaneous value of the spatial distribution of (mmf) produced by one phase current defined in Figure 17.

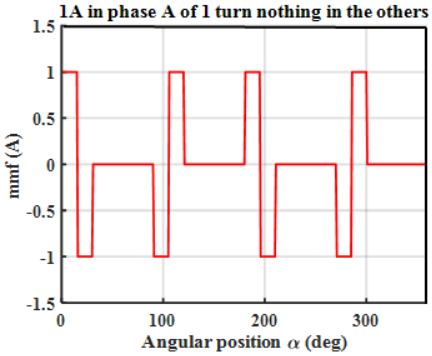

Figure 17: Spatial distribution of the magnetomotive force created by current 1A in phase A.

This curve can be decomposed into Fourier series considering the superposition of 8 pulses of 15° width. For each pulse the calculation is known, we must add the eight series of Fourier with the right phase shifts: $\theta_1 = \pi/24$ which locates the center of the first tooth. The centers of the seven other impulses are located at $\theta_2 = 3\pi/2\,4$, $\theta_3 = 13\pi/24$, $\theta_4 = 15\pi/24$,$\theta_5 = 25\pi/24$, $\theta_6 = 27\pi/24$, $\theta_7 = 37\pi/24$ and $\theta_8 = 39\,\pi/24$.

For a centered impulse (pair function and no sliding symmetry), the coefficient of rank n of the Fourier series is written:

$$a_n = \frac{2}{n\pi}\sin\left(n\frac{\pi}{24}\right) \tag{4}$$

The Fourier series of the mmf phase A is obtained by adding the elementary functions by taking the previously calculated phase shifts. The complex writing is less heavy; the signs of the impulses are taken into account in the sum of the 8 terms. The result is:

$$A_n = N.i_U[a_n\,exp(-jn\theta_1) - a_n\,exp(-jn\theta_2) - a_n\,exp(-jn\theta_3) + a_n\,exp(-jn\theta_4) + a_n\,exp(-jn\theta_5) - a_n\,exp(-jn\theta_6) - a_n\,exp(-jn\theta_7) + a_n\,exp(-jn\theta_8)] \quad (5)$$

A Matlab script computes harmonics up to rank 100 to get a realistic recomposition of the mmf. The amplitudes of the spectrum lines are given in Figure 18 until to rank 20 for phase A. mmfs of phases B and C have the same amplitudes with different phase-shift.

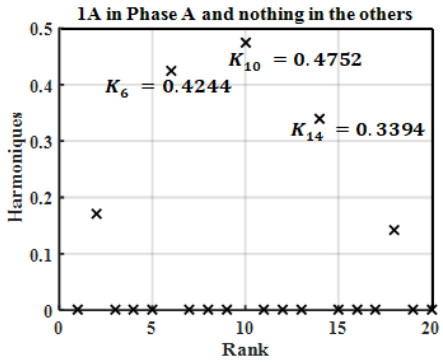

Figure 18: Spectrum lines of the mmf produced by 1 A in the phase A.

This figure shows that the chosen winding creates a preponderant spatial harmonic of rank 10. When this winding is associated with a rotor with 10 pairs of poles, an average torque is produced. Other rays do not create average torque but harmonics torques. This is the main disadvantage of the concentrated winding motor. Calculations are verified by recomposing the spatial distribution of mmf for each phase from their Fourier series. Figure 19 shows the results obtained and the positioning of the sinusoid representing the harmonic 10, which produces the average torque. It also represents the recomposition of the spatial distribution of the mmf for complete turn (360°). It can be seen that the spatial harmonic of rank 10 has 10 periods on turn.

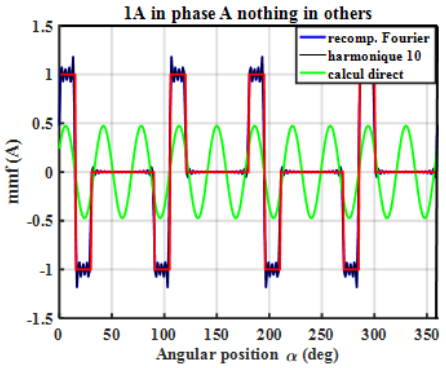

Figure 19: mmf when phase A is supplied.

Figure 20 is a zoom of the green curve of the previous figure it shows the first period of the harmonic of rank 10 of the spatial distribution of the mmf which creates the torque keeping the same position of the reference axis α

= 0. The spatial distributions of the fmm produced by the other phases are similar but spatially shifted by 12°.

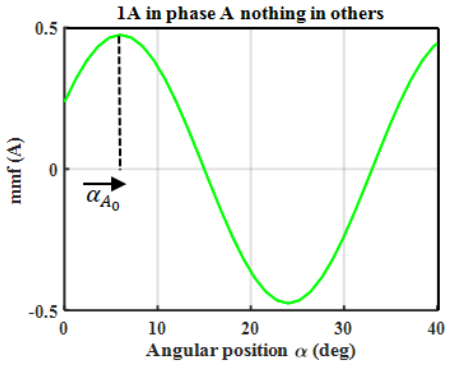

Figure 20: One period of the recomposition of the spatial distribution of the mmf.

Figure 20 allows formulating the expression of the fmm of rank 10 which is a sinus of period $\frac{2\pi}{10}$ shifted by (6°)

$$\varepsilon_A(\alpha) = K_{10}\, N i_A \cos\left(10\left(\alpha - \frac{\pi}{30}\right)\right) \tag{6}$$

The same approach done for the other phases:

$$\varepsilon_B(\alpha) = K_{10}\, N i_B \cos\left(10\left(\alpha - \frac{\pi}{10}\right)\right) \tag{7}$$

$$\varepsilon_C(\alpha) = K_{10}\, N i_C \cos\left(10\left(\alpha - \frac{\pi}{6}\right)\right) \tag{8}$$

The resulting fmm is obtained by superposition

$$\varepsilon(\alpha) = K_{10}\, N\left\{i_A \cos\left(10\left(\alpha - \frac{\pi}{30}\right)\right) + i_B \cos\left(10\left(\alpha - \frac{\pi}{10}\right)\right) + i_C \cos\left(10\left(\alpha - \frac{\pi}{6}\right)\right)\right\} \tag{9}$$

When the three phases are supplied with sinusoidal by Three-phase electric power system at the frequency f, the currents are written:

$$\begin{aligned} i_A &= I\sqrt{2}\cos(\omega t) \\ i_B &= I\sqrt{2}\cos\left(\omega t - \frac{2\pi}{3}\right) \\ i_C &= I\sqrt{2}\cos\left(\omega t - \frac{4\pi}{3}\right) \end{aligned} \tag{10}$$

By substituting the expressions of the currents in the formula of the mmf, after simplification, it comes;

$$\varepsilon(\alpha, t) = K_{10}\, NI\sqrt{2}\,\frac{3}{2}\cos\left(\omega t - 10\alpha + \frac{\pi}{3}\right) \tag{11}$$

This expression allows locating a point where the mmf is maximum.

$$\alpha(t) = \frac{\omega t + \pi/3}{10} \tag{12}$$

The harmonic 10 of the mmf spatial distributions create a rotating field with 10 pole-pairs capable of driving the rotor at the speed ω / 10. The same calculations made with the other harmonic components of the mmf spatial distribution make it possible to calculate the sequences and amplitudes of the main mmf created by the winding. The results are shown in Table 1.

Table 1: Rank sequences and amplitudes of all the harmonic components of the mmf spatial distribution.

Rank	Sequence	Amplitude (A)	Coefficient	Initial position (rd)
6	homopolar	0	$K_6 = 0.4244$	-
10	direct	$\frac{3\sqrt{2}\,K_{10}\,NI}{2}$	$K_{10} = 0.475$	$\frac{\pi}{30}$
14	inverse	$\frac{3\sqrt{2}\,K_{14}\,NI}{2}$	$K_{14} = 0.339$	$\frac{\pi}{21}$

Figure 21 shows the rotating (mmf) of rank 10 which produces the motor torque and which rotates in the direct direction while Figure 22 shows (mmf) of rank 14 which turns in the opposite direction and which disturbs the operation.

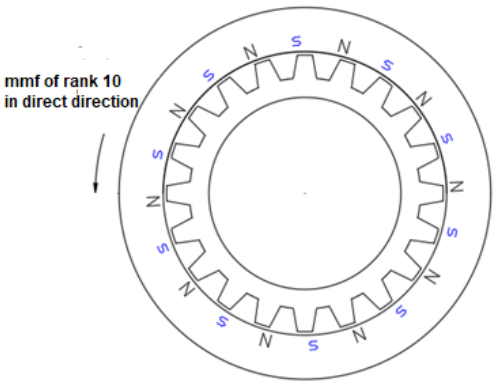

Figure 21: mmf of rank 10 which produces torque and turns in the direct direction.

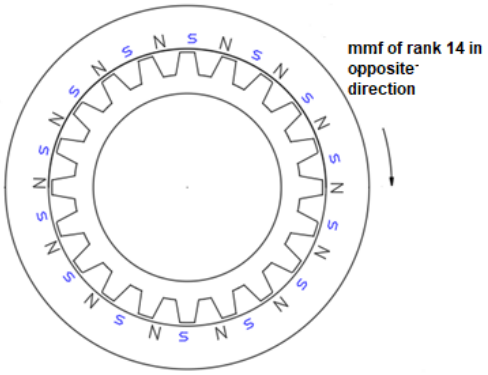

Figure 22: mmf of rank 14 which turns in the opposite direction.

These fixed and rotating mmf exist simultaneously, they create inductions that are superimposed in the air gap. The study is limited to the main harmonics rank 10 and 14. The maximum amplitude of the field is obtained at the points and at the moment when all the mmf adds up and when this point is located in front of the rotor tooth. For the motor to work in linear mode, it is necessary that this point creates an induction lower than the saturation knee of the magnetic material.

4. Maximum current corresponding to saturation

The spatial distribution of the mmf makes it possible to estimate the distribution of the induction when the permeance of the air gap is known. For doubly salient switched reluctance motor the maximum induction is obtained at positions where the rotor tooth is in front of stator tooth. For this point, the equivalent diagram in Figure 23 makes it possible to estimate the mmf corresponding to the maximum induction that must stay in the linear zone. In this figure R is the average radius of the air gap, e_0 its thickness and l length of the motor. The relative permeability of the sheets is assumed to be very high.

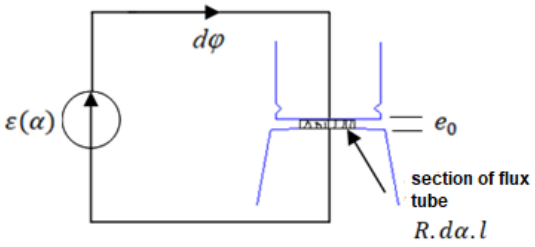

Figure 23: Schematization of flux tube in one tooth with the equivalent diagram.

Flux tube permeability is written:

$$dp = \mu_0 \frac{R.d\alpha.l}{e_0} \tag{13}$$

Therefore the flux in the tube is written:

$$d\varphi = \mu_0 \frac{R.l.d\alpha}{e_0}.\varepsilon \tag{14}$$

On the other hand

$$\varphi_{max} = B_{max}.ds = B.Rd\alpha.l \tag{15}$$

$$B_{max} = \frac{d\varphi_{max}}{Rld\alpha} \tag{16}$$

By Substitution (14) in (16):

$$B = \mu_0 \frac{\varepsilon}{e_0} \tag{17}$$

To avoid motor saturating we have to limit the peak value of the fmm to:

$$\varepsilon_{max} = \frac{B_{\max} e_0}{\mu_0} \tag{18}$$

In this motor the main components of the rotating mmf are the harmonic of rank 10 (forward wave) and the harmonic of rank 14 (backward wave). For a fixed point of the air gap these rotating quantities are superimposed. There are moments when their amplitudes are added. To stay in the linear zone, the induction corresponding to the sum of these two components must be less than the induction of saturation of the magnetic core B_{sat} .

$$B_{10_{max}} + B_{14_{max}} < B_{sat} \tag{19}$$

$$\frac{3\sqrt{2}NI}{2} \frac{\mu_0}{e_0} (K_{10} + K_{14}) < B_{sat} \tag{20}$$

The result is *NI*=645 (*At*) for $B_{sat} = 2.2T$ with cobalt iron core and air gap $e_0 = 0.7mm$. The turn number of each coil is computed at full speed (5000*rpm*) considering the cross section of slots and the series connection of 8 coils for a phase. The result is 24 turns for a standard of 230 *Vrms*. The prototype is built with non-organic coils molded in HT° cement. For technological reasons the wire diameter is 1 mm. To stay in linear operation at the most unfavorable points the current must be limited to 26 *Arms*, which corresponds to a current density of 33 A/mm^2. This very high current density is possible with HT° coils and a standard cooling. A general view of the HT° motor is shown in Figure 24. This motor has a stainless steel carcass and the bearing made in ceramic to resist the high temperature.

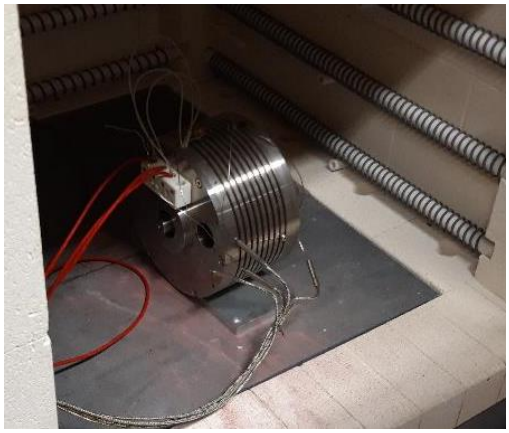

Figure 24: A general view of the HT° motor

5. Conclusions

The presented approach allows defining the main parameters of doubly salient synchronous reluctance motor able to work up to 500°C at the heart of the coils. The choice of the number of stator teeth is imposed for practical reasons of stator availability. The numerical study allows defining the number of teeth of the rotor and their forms. The machine is designed for working in linear magnetic conditions; the average torque is produced by the rotating stator mmf of rank 10 which has 20 poles. The analytical study yields the magnitude and phase for every rotating mmf due to space harmonics. Therefore, it is possible to compute the maximum current corresponding to the magnetic saturation. The reluctance machine control needs an accurate knowledge of the relative position of the active mmf rotating wave and the rotor poles; the analytical study yields a simple relation between the mmf wave position and the stator current. The rotor position is measured by a specific HT° sensor. The next step is the analysis of the winding fast transients due to the steep-fronted voltage imposed by the feeding inverter.

References

[1]. L. Prisse, D. Ferer, H. Foch, A. Lacoste, “New power centre and power electronics sharing in aircraft,” 13th European Conference on Power Electronics and Applications, Sept. 2009, pp. 1-9.

[2]. J. W. Bennet, G. J. Atkinson, B. Mecrow, and D. J. Atkinson, “Fault tolerant design considerations and control strategies for aerospace drives”, IEEE Trans. Ind. Electron., vol. 59, no. 5, pp. 2049–2058, May 2012.

[3]. Guynn, M. D., Berton, J. J., Haller, W. J., Hendricks, E. S., and Tong, M. T., “Performance and Environmental Assessment of an Advanced Aircraft with Open Rotor Propulsion,” NASA/TM-2012-217772, NASA Langley Research Center, Hampton, VA, 2012.

[4]. Van Zante, D.E., Gazzaniga, J. A., Elliott, D.M., and Woodward, R. P., “An Open Rotor Test Case: F31A31 Historical Baseline Blade Set,” ISABE 2011-1310, International Society of Air Breathing Engines, Gothenburg, Sweden, Sept 2011.

[5]. Vadim Iosif, Noureddine Takorabet, Daniel Roger, Stéphane Duchesne, Farid Meibody-Tabar. Conception d'un prototype de machine Ultra-Haute Température (500°C). Symposium de Genie

Electrique, Jun 2016, Grenoble, France.

[6]. Vadim Iosif, Daniel Roger, Noureddine Takorabet, Stéphane Duchesne, Farid Meibody-Tabar. Technological assessments for designing machines able to work at very high internal temperatures (450-500°C). XX11 Int. Conf. On Elec. Machines ICEM'2016. PP. 2682-2687, Sept 2016, Lausanne Suizerland.

[7]. A. De Vries, M. Gabsi, Y. Bonnassieux, M. Lecrivain, M. Le Pinçart, and C. Plasse, "Fonctionnement moteur et générateur des MRVDS. Application aux alterno-démarreurs, " EJEE, Vol. 7, No 5-6, 2004, pp.613-639.

[8]. T.J.E. Miller, Electronic control of switched reluctance machines. Oxford, England: Newnes, 2001.

[9]. KANT Michel , "Les actionneurs électriques pas à pas", Traité des nouvelles technologies, série automatique, Hermès 1989

[10]. JUFER, "Electromécanique", Traité de l'école polytechnique fédérale de Lausanne, Ed. Georgi(1979).

[11]. J. Chatelain, Machines électriques , Traité d'Electricité, Volume X, Presses Polytechniques Romandes, Lausanne, 1983, 628p.

[12]. J. Lesenne, F. Notelet and G. Seguier, Introduction à l'électrotechnique approfondie, Technique et Documentation, Paris, 1981, 247p.